Journal of
Materials Chemistry A

PAPER

View Article Online
View Journal | View Issue

Cite this: *J. Mater. Chem. A*, 2022, **10**, 6216

Impact of the dopant-induced ensemble structure of hetero-double atom catalysts in electrochemical NH_3 production†

Seung-hoon Kim,[ab] Ho Chang Song,[c] Sung Jong Yoo,[ade] Jonghee Han,‡*[ab] Kwan-Young Lee *[bf] and Hyung Chul Ham *[c]

Using spin-polarized density functional theory (DFT) calculations, we examined electrochemical N_2 reduction (N_2RR) toward NH_3 production on hetero-RuM (M = 3d transition metals) double atom catalysts supported on defective graphene by means of analysis on the geometric ensemble structure, the N_2RR mechanism, the decoupling of strain, dopant and configurational effects and the d-orbital resolved density of states (ORDOS) (d_{z^2}, d_{xz}, d_{yz}, d_{xy}, and $d_{x^2-y^2}$) on the hetero-double atoms. In addition, we computationally screened novel catalysts by exploring 4d, 5d and p block metals as the hetero-M metals in the RuM system. First, we found the significantly enhanced N_2RR activity of inclined pentagon M (Fe, Mn, and Sc) double atom catalysts (RuFe has the highest activity) compared to the homo-Ru_2 double atom catalyst. Our DFT calculations on the interplay of strain, dopant and configurational effects in the inclined pentagon M (Fe, Mn, and Sc) double atom catalysts predicted that (1) the dopant effect was the promoter to improve the N_2RR activity of RuSc and RuMn, (2) the tensile strain (RuSc) tended to reduce the NH_3 productivity *via* the N_2RR, while the effect of compressive strain (RuFe and RuMn) was insignificant, and (3) the dopant-support interaction induced a unique inclined pentagon M double atom ensemble structure, which leads to the large reduction of the N_2RR activity of the hetero-RuSc double atom but the activity increases for the hetero-RuFe and RuMn cases. Finally, our DFT calculation on the analysis of the p–d (d_{z^2}, d_{xz}, d_{yz}, d_{xy}, and $d_{x^2-y^2}$) orbital overlap identified the key d orbitals in determining the descriptor (NH_2 adsorption energy) for representing the N_2RR. That is, the orbitals (d_{z^2}, d_{xz}, and d_{yz}) having an orientation toward the *z* direction in the horizontal Ru_2 double atom played an important role in determining the NH_2 adsorption process, while for the inclined pentagon M double atoms (RuFe, RuSc, and RuMn), the d_{xz} and d_{xy} orbitals were found to be essential for the modification of NH_2 adsorption energy. Finally, a descriptor based DFT search additionally discovered promising hetero-RuOs and RuIr double atom catalysts. This study highlights that the dopant engineering of hetero-double atom catalysts supported on defective graphene can significantly modify the electrochemical reactivity, particularly by the dopant type and geometric ensemble structure.

Received 27th September 2021
Accepted 7th January 2022

DOI: 10.1039/d1ta08358a

rsc.li/materials-a

Introduction

To reduce global warming, many studies are being actively conducted around the world to reduce anthropogenic carbon dioxide (CO_2) emissions and find new clean energy sources to replace fossil fuels. Among the candidates for new energy media, hydrogen (H_2) is being spotlighted.[1] H_2 is the most bountiful chemical substance in the universe, and it is colourless, non-toxic and highly combustible. It can be produced without carbon emission through electrolysis of water using renewable electricity and used as a power source for fuel cells that can produce electricity for ships, airplanes, automobiles, and drones.[2–4] When H_2 is consumed in a fuel cell, it only emits water as a byproduct.[5] However, its low volumetric energy density, wide range of flammability limits, and high

[a]Center for Hydrogen and Fuel Cell Research, Korea Institute of Science and Technology (KIST), 5, Hwarangno 14-gil, Seongbuk-gu, Seoul, 02792, Republic of Korea

[b]Graduate School of Energy and Environment, Korea University, 145, Anam-ro, Seongbuk-gu, Seoul, 02841, Republic of Korea

[c]Department of Chemistry and Chemical Engineering, Education and Research Center for Smart Energy and Materials, Inha University, 100, Inha-ro, Michuhol-gu, Incheon, 22212, Republic of Korea. E-mail: ham.hyungchul@inha.ac.kr

[d]KHU-KIST Department of Converging Science and Technology, Kyung Hee University, Seoul 02447, Republic of Korea

[e]Division of Energy & Environment Technology, KIST School, University of Science and Technology (UST), Seoul 02792, Republic of Korea

[f]Department of Chemical and Biological Engineering, Korea University, 145, Anam-ro, Seongbuk-gu, Seoul, 02841, Republic of Korea. E-mail: kylee@korea.ac.kr

† Electronic supplementary information (ESI) available. See DOI: 10.1039/d1ta08358a

‡ Current address: Korea Institute of Energy Technology (KENTECH), Naju-si, Jeollanam-do, 58330, Republic of Korea. E-mail: jhan@kentech.ac.kr

transportation cost are obstacles to using it directly as an energy medium.

Recently, ammonia (NH_3) has been prominent as a promising candidate for storage and transportation of H_2 due to its several advantages. It can be readily liquefied under 8 bar at ambient temperature,[6] and its relatively high autoignition temperature (651 °C, compared to 254 °C for diesel) enables us to use it safely from fire and explosion.[7–9] Zamfirescu *et al.* reported that NH_3 is competitive compared to other common fuels such as gasoline, liquefied petroleum gas (LPG) and methanol due to its high volumetric and gravimetric H_2 storage density and low energy costs.[7] It is already widely used for industrial use and has a distributional infrastructure to transport it in amounts larger than 100 million tons yearly or more.[10]

In industrial NH_3 production so far, the Haber–Bosch process constitutes the dominant route.[11,12] However, this process consumes a huge amount of energy due to its high operating temperatures (400–500 °C) and pressure (150–300 bar) to break the intermolecular N≡N bond, which is equivalent to about 2% of the worldwide energy use.[13,14] Moreover, natural gas (mainly methane) is used as a source of H_2, releasing massive amounts of CO_2 as a by-product.

In contrast, electrochemical NH_3 production through the N_2 reduction reaction (N_2RR) can synthesize NH_3 directly from N_2 and H_2 without carbon emission, and it can be operated by supplying renewable electricity such as solar and wind power. In general, electrolytic cells based on a solid electrolyte membrane are used for this process as they allow easy separation of the H_2 feed from the NH_3 product.[15,16] The basic equations for electrochemical NH_3 production using electrolytic cells under acidic conditions are as follows:

Anode:

$$3H_2O \rightarrow 3/2O_2 + 6H^+ + 6e^-$$

Cathode:

$$N_2 + 6H^+ + 6e^- \rightarrow 2NH_3$$

Overall:

$$N_2 + 3H_2O \rightarrow 3/2O_2 + 2NH_3$$

In the anode, water (H_2O) is oxidized through the oxygen evolution reaction, giving protons and electrons and releasing oxygen. These protons and electrons are transferred to the cathode *via* the membrane and electric potential, respectively. In the cathode, NH_3 is produced by the N_2RR, in which gaseous N_2 is sequentially combined with protons and electrons.

Group VIII elements (Fe, Ru and Os) have been known to have excellent activity in electrochemical NH_3 production.[17–22] In addition, the catalyst research has been expanded to noble metals (*e.g.* Rh, Pd, Au, Ru, Pt and their oxides, nitrides, and sulphides), non-noble metals (*e.g.* Ti, Fe, Ni, Mo, V, W and their oxides, nitrides and sulphides), and carbon-based non-metal catalysts.[23–39] Among those species, Ru has been reported to be the most active catalyst. For example, according to Nørskov's study, there is a volcanic relationship between the number of valence electrons and the NH_3 productivity, indicating that Ru has optimal valence electrons for NH_3 production through N_2 reduction.[20] Ru has exhibited a high reactivity toward electrochemical NH_3 production under room temperature and pressure conditions.[11,15,16,21,22] However, Ru still shows poor NH_3 productivity for the commercialization of electrochemical NH_3 production.

To deal with this issue, the concept of single atom catalysts (SACs) has been recently introduced to make a breakthrough in activity for electrochemical NH_3 production, since it can improve activity beyond the existing volcanic curve, maximize the number of active sites, and achieve economic feasibility by reducing catalyst loading.[40–47] Zhao *et al.* theoretically reported that single Mo exhibited the lowest N_2RR onset potential (−0.35 V) among SACs embedded in defective boron nitride sheets,[40] and Lü *et al.* claimed that the active site for the N_2RR on an Fe catalyst anchored to an N-doped carbon framework is Fe–N–C, in which a single Fe atom is bonded to four N atoms.[42] For Ru-based SACs, Geng *et al.* reported that Ru–N–C SACs showed a lower overpotential [$\Delta G(Ru_1–N_3) = 0.73$ eV and $\Delta G(Ru_1–N_4) = 0.77$ eV] compared to the Ru (101) catalyst [$\Delta G = 0.91$ eV] by using calculations and experiments.[47] This study showed that Ru SACs supported on N-doped graphene have better activity than metallic Ru catalysts for the N_2RR. However, they did not discuss the origin of the enhanced N_2RR activity in detail.

In the catalytic design, the introduction of hetero-atoms into a pure metal (so-called alloy or multi-metallic catalysts) has been known as a salient approach for the enhancement of catalyst activity and durability: for example, core@shell, surface alloys, and intermetallic alloys.[48–50] Nonetheless, a study on the heteroatom addition strategy has not yet been conducted to tune the activity of a single atom catalyst.

In this study, the electrochemical activity of Ru-based SACs, homo-Ru_2 double atom catalysts (DACs), and hetero-RuM DACs having Ru and M (M = 3d transition metal) was investigated using quantum mechanics computation based on spin-polarized density functional theory (DFT). We calculate the structural stability, reaction mechanism and activity of the N_2RR on homo- and hetero-Ru DACs. In addition, the decoupling of strain, dopant and configurational effects and the d-orbital resolved density of states (ORDOS) (d_{z^2}, d_{xz}, d_{yz}, d_{xy}, and $d_{x^2-y^2}$) on the hetero-double atoms are presented for a clear understanding of enhanced catalysis. Finally, using the descriptor we have identified, we computationally screen for a novel catalyst composition by exploring more search spaces (4d, 5d, and p block metals) for boosting NH_3 production *via* N_2 reduction.

Computational details

All of the calculations were performed on the basis of spin-polarized density functional theory (DFT) as implemented in the Vienna *Ab initio* Simulation Package (VASP).[51–53] The projector augmented wave (PAW) method using a plane wave basis set was implemented to describe the interaction between core and valence electrons.[54] The Perdew–Burke–Ernzerhof (PBE) exchange-correlation functional within the generalized gradient approximation (GGA) was employed.[55] For the plane wave expansion of the electronic eigenfunctions, an energy cutoff of 400 eV was used.

To model the RuM/C catalysts, we first built a periodic geometry of monolayer graphene consisting of 60 carbon atoms from a $P6_3/mmc$-structured graphite supercell by removing all layers except one and stretching the z vector to 20 Å.[56] After modelling of pristine graphene, two adjacent carbon atoms were removed to create unsaturated carbon to provide embeddable sites for Ru and 3d transition metal (M) atoms.

Here, we chose defective graphene as the supporting material for DACs instead of pristine graphene. Note that the interaction between pristine graphene and DACs is not strong enough to prevent the aggregation of DACs.[57] According to Jamie H. Warner *et al.*, an Fe double atom in defective graphene has been successfully incorporated *via* the defect-assisted doping method by electron beam irradiation.[58] That is, the Fe precursor ($FeCl_3$) solutions are added on the surface of graphene *via* drop-casting and in turn vacancy sites are created through irradiation with a focused electron beam using an aberration-corrected transmission electron microscope (AC-TEM), leading to an Fe dimer (Fe double atom) embedded into defective graphene.[59,60] In addition, Pt dimers can be prepared on defect-rich graphene using atomic layer deposition (ALD), through the creation of nucleation sites, single Pt atom deposition and attachment of a second Pt atom selectively on the single Pt one.[61] Following these considerations and computational validation, the RuM/C catalysts were modelled by using mono- and diatomic clusters anchored to defective graphene with double vacancies (see Fig. S1†).

To find the optimized geometry and the total energy of hetero-RuM DACs, all of the atoms were fully relaxed using the conjugate gradient method until residual forces on all the constituent atoms became smaller than 5×10^{-2} eV Å^{-1}.[62] For Brillouin zone integration, we chose a $(4 \times 4 \times 1)$ Monkhorst–Pack mesh of k-points to determine the equilibrium geometries and total energies of RuM/C catalysts.[63] To calculate the electronic structure, average energy and occupancy of the d-band, and atomic charge density of the catalysts, we increased the mesh size to $(10 \times 10 \times 1)$.

In the total N_2RR process ($N_2 + 6(H^+ + e^-) \rightarrow 2NH_3$), N_2 is reduced to NH_3 through six net coupled proton and electron (CPE) transfer steps, and each step involves the transfer of a CPE from solution to an adsorbed intermediate.[39] To calculate the Gibbs free energy change (ΔG) of every step for the N_2RR, we introduced a computational hydrogen electrode (CHE) model as pioneered by Nørskov.[64] In this model, the free energy of a CPE is equivalent to half that of gaseous H_2 [$G(H^+ + e^-) = 1/2G(H_2)$] under standard reaction conditions ($T = 298.15$ K, $P = 1$ bar, and pH $= 0$) with no external potential. According to this method, the ΔG value can be determined using the following equation;

$$\Delta G = \Delta E - T\Delta S + \Delta ZPE - neU$$

where ΔE, ΔS, ΔZPE, n, and U are the total energy difference directly obtained from DFT calculations, the entropy change, the change in zero-point energies, the number of electrons transferred during the reaction, and the operating electrochemical potential in the SHE, respectively. The entropies and zero-point energies of the N_2RR intermediates were computed from the vibrational frequencies, in which the adsorption vibrational mode was calculated explicitly with all atoms fixed except for N_2RR intermediates, metal atoms, and carbon atoms bonded with metal atoms.[65] The entropies of gaseous molecules under reaction conditions were taken from the NIST Chemistry WebBook.[66]

Results and discussion

Mechanism of electrochemical NH_3 production on Ru single and double atom catalysts

According to previous studies,[13,45,46,67–69] the NH_3 formation paths from the electrochemical N_2RR on a SACs can be mainly classified into two reaction routes: the dissociative and associative mechanisms, which are shown in Fig. 1. The first step for both the dissociative and associative mechanisms is the adsorption of a gaseous N_2 molecule in the catalyst [(1) $N_2(g) \rightarrow N_2{}^*$] (the asterisk * denotes the end-on adsorption state). In the dissociative mechanism, the adsorbed N_2 molecule ($N_2{}^*$) is dissociated into two N* atoms on the catalytic surface [(2) $N_2{}^* \rightarrow 2N^*$], which can then undergo three successive protonation reactions, leading to NH_3 production [(3) $N^* + (H^+ + e^-) \rightarrow NH^*$, (4) $NH^* + (H^+ + e^-) \rightarrow NH_2{}^*$, and (5) $NH_2{}^* + (H^+ + e^-) \rightarrow NH_3(g)$]. On the other hand, in the associative mechanism, $N_2{}^*$ is protonated to form N_2H^* [(6) $N_2{}^* + (H^+ + e^-) \rightarrow N_2H^*$], which undergoes protonation or protonolysis (the cleavage of the N–N bond by the addition of H^+) for NH_3 formation. Here, depending on the type of catalyst, the reduction of N_2H to NH_3 follows one of the following three reaction pathways: (A) alternating path [(7) $N_2H^* + (H^+ + e^-) \rightarrow HN_2H^*$, (8) $HN_2H^* + (H^+ + e^-) \rightarrow HN_2H_2{}^*$, (9) $HN_2H_2{}^* + (H^+ + e^-) \rightarrow H_2N_2H_2{}^*$, and (10) $H_2N_2H_2{}^* + (H^+ + e^-) \rightarrow NH_2{}^* + NH_3(g)$], (B) distal path [(11) $N_2H^* + (H^+ + e^-) \rightarrow N_2H_2{}^*$ and (12) $N_2H_2{}^* + (H^+ + e^-) \rightarrow N^* + NH_3(g)$] and (C) enzymatic path (unlike alternating and distal paths, N_2 is adsorbed on the catalyst surface *via* a side-on configuration) [(13) $^*N_2H^* + (H^+ + e^-) \rightarrow {}^*HN_2H^*$, (14) $^*HN_2H^* + (H^+ + e^-) \rightarrow {}^*HN_2H_2{}^*$, (15) $^*HN_2H_2{}^* + (H^+ + e^-) \rightarrow {}^*H_2N_2H_2{}^*$, and (16) $^*H_2N_2H_2{}^* + (H^+ + e^-) \rightarrow NH_2{}^* + NH_3(g)$ (note that double asterisks ** denote the side-on states of adsorbates)]. In addition, the N_2RR can also follow a mixed mechanism of

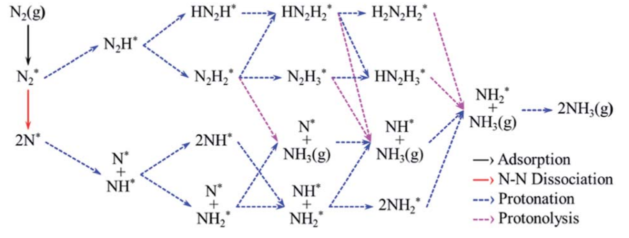

Fig. 1 Detailed N_2RR pathway considered in this study.

alternating, distal and enzymatic pathways [(17) $*HN_2H_2* + (H^+ + e^-) \rightarrow NH* + NH_3(g)$ and (18) $N_2H_2* + (H^+ + e^-) \rightarrow HN_2H_2*$].

Here, we considered the $NH_2* + (H^+ + e^-) \rightarrow NH_3(g)$ reaction as the final reaction step in the N_2RR, where the NH_3 desorption energy is indirectly included in the NH_2* protonation reaction. Note that the $NH_2* + (H^+ + e^-) \rightarrow NH_3(g)$ reaction is considered to be the combination of $NH_2* + (H^+ + e^-) \rightarrow NH_3*$ and $NH_3* \rightarrow NH_3(g)$, which makes it possible to understand the electrode potential effect on the NH_3 desorption process.[69]

In this study, we first attempt to determine the preference of the dissociative mechanism in the N_2RR by calculating the free energy change for the $N_2(g) \rightarrow N* + N*$ reaction (ΔG_{diss}) using the following equation.

$$\Delta G_{diss} = 2G(N*) - [G(N_2) + 2G(bare)]$$

where $G(N_2)$, G(bare) and $G(N*)$ indicate the free energies of the gaseous N_2 molecule, the bare catalyst without N*, and the adsorbed N*, respectively.

If the ΔG_{diss} value (which can be used to understand what type of N_2RR mechanism takes place more favourably) on the catalytic surface is positive (endothermic process), the dissociative mechanism may not be possible for the N_2RR to NH_3. A negative ΔG_{diss} value means that N* is more stable than N_2*, indicating that the N_2RR may follow the dissociative mechanism. Here, we further confirm whether the catalyst having a negative ΔG_{diss} value goes through the dissociative mechanism by calculating the barrier (ΔG_{barr}) for the N_2 dissociation reaction into 2N*.

Fig. 2 displays the most favourable N_2RR pathways and optimized geometric structures of intermediates in each reaction step on the Ru_1 SACs and homo-Ru_2 DACs. For the Ru_1 SAC case, the N_2RR is found to follow the associative 'Distal' mechanism (note that ΔG_{diss} = 2.07 eV, indicating that the dissociative mechanism is unfavourable). First, a N_2 molecule is adsorbed on top of the Ru atom in an end-on configuration [(1) $N_2(g) \rightarrow N_2*$] and then undergoes two successive protonation reactions to form $*N_2H*$ with a side-on configuration [(6) $N_2* + (H^+ + e^-) \rightarrow *N_2H*$] and N_2H_2* [(11) $*N_2H* + (H^+ + e^-) \rightarrow N_2H_2*$] with an end-on configuration. Here, the N–N bond length of $N_2(g)$, N_2*, $*N_2H*$, and N_2H_2* is 1.12 Å, 1.13 Å, 1.25 Å, and 1.31 Å, respectively. Next, the adsorbed N_2H_2* dissociates into N* and $NH_3(g)$ by protonolysis [(12) $N_2H_2* + (H^+ + e^-) \rightarrow N* + NH_3(g)$]. Finally, $NH_3(g)$ is formed by three successive protonation reactions of adsorbed N*. This is consistent with prior reports on single atom catalysis.[40–42,45–47]

On the other hand, our DFT calculation predicts that the homo-Ru_2 DAC follows a mixed mechanism of 'Alternating' or 'Distal' and 'Enzymatic' pathways (note that ΔG_{diss} = 1.24 eV). First, a N_2 molecule is adsorbed on top of a single Ru atom in the Ru_2 DAC with an end-on configuration, which leads to side-on $*N_2H*$ formation by protonation. Next, $*N_2H*$ undergoes two successive protonation reactions to form $*HN_2H*$ [(7) $*N_2H* + (H^+ + e^-) \rightarrow *HN_2H*$] and $*HN_2H_2*$ [(8) $*HN_2H* + (H^+ + e^-) \rightarrow *HN_2H_2*$]. The N–N bond length in N_2*, N_2H*, HN_2H*, and HN_2H_2* is 1.14 Å, 1.28 Å, 1.37 Å, and 1.46 Å, respectively. Finally, $*HN_2H*$ is decomposed into $NH_3(g)$ + NH* by the protonolysis of the N–N bond [(17) $*HN_2H_2* + (H^+ + e^-) \rightarrow NH* + NH_3(g)$] and then NH* is converted into $NH_3(g)$ *via* two successive protonation reactions.

The calculated free energy diagrams for the N_2RR to NH_3 on the Ru SAC and homo-Ru_2 DAC are displayed in Fig. 3. The

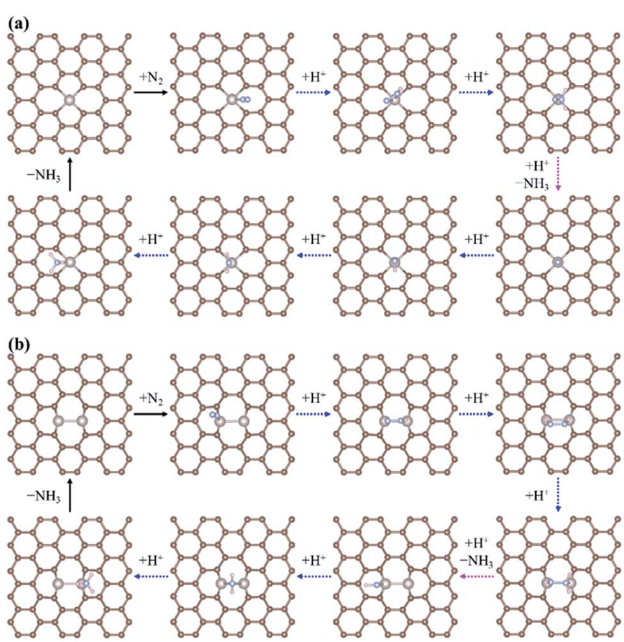

Fig. 2 The optimized geometric structures of N_2RR intermediates along the most favourable reaction pathway on (a) the Ru SAC and (b) the homo-Ru_2 DAC.

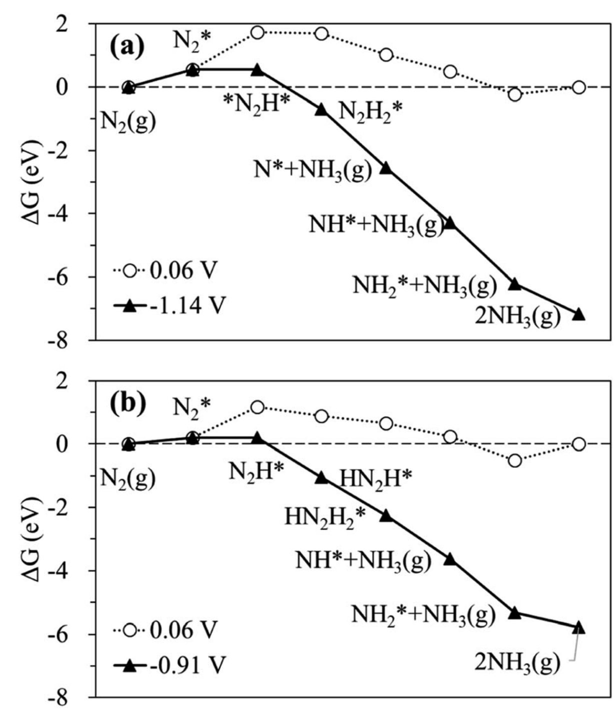

Fig. 3 Calculated free energy profiles at equilibrium (○) and limiting (▲) potentials for the N_2RR on (a) the Ru SAC and (b) the homo-Ru_2 DAC *via* the most favourable pathway.

adsorption energies (ΔE_{ads}) are calculated as follows: [$\Delta E_{ads}(X) = EX^* - (E(bare) + E(X))$], where EX^*, E(bare), and E(X) denote the total energy of the X-adsorbed surface, the bare surface, and the isolated X species, respectively. E(X) was calculated in a cubic vacuum unit cell of size $a = 20$ Å, and the calculated E(X) values are shown in Table S1.† For both the Ru_1 SAC and the homo-Ru_2 DAC, the N_2 adsorption under thermodynamic equilibrium potential conditions (0.06 V) is predicted to be an endothermic process, which comes from the large loss of entropy due to the formation of a bound state.[68] Note that $\Delta G = 0.54$ eV and $\Delta E_{ads}(N_2) = -0.46$ eV for the Ru_1 SAC, and $\Delta G = 0.21$ eV and $\Delta E_{ads}(N_2) = -0.84$ eV for the homo-Ru_2 DAC. For the N_2RR under thermodynamic equilibrium potential conditions for both the Ru_1 SAC and homo-Ru_2 DAC, the first step [(6) $N_2^* + (H^+ + e^-) \rightarrow {}^*N_2H^*$] is calculated to be the most endothermic [note that $\Delta G =$ 1.14 eV (Ru_1 SAC) and 0.91 eV (Ru_2 DAC)] among all the steps for the most favourable N_2RR pathway. This indicates that the first N_2 protonation [which is defined as the potential limiting step (PLS)] determines the NH_3 production potential. Consequently, for the Ru_1 SACs and homo-Ru_2 DACs, we predict an over-potential of 1.19 V and 0.96 V, respectively, suggesting the higher N_2RR activity of a homo-Ru_2 DAC than a Ru_1 SAC. This is higher than previous single Ru atom calculation results,[47] which shows that the overpotentials for Ru_1–N_3 and Ru_1–N_4 are predicted to be 0.79 V and 0.83 V, respectively. This difference is related to the presence of N atoms in the defective graphene support. In our DFT study, a single Ru atom is embedded into a defective graphene support (forming a Ru–C bond), while, in the previous calculation, single Ru atoms are associated with three N atoms (Ru_1–N_3) or four N atoms (Ru_1–N_4) in the defective graphene support (forming a Ru–N bond). Due to the higher electronegativity of the N atom (3.04) than the carbon case (2.55), the Ru in the Ru–N bond loses more electrons than that in the Ru–C case, which may lead to the increase of adsorption strength in reaction intermediates and in turn the enhancement of N_2RR activity.

Next, we examine the effect of the addition of a hetero-M atom (M = Sc, Ti, V, Cr, Mn, Fe, Co, Ni) into a Ru_1 SAC in order to enhance the N_2RR activity toward NH_3 formation.

Geometric ensemble structure of hetero-RuM double atom catalysts

First, we investigate the structural stability of hetero-RuM DACs supported on defective graphene by calculating the formation energy (indicated as ΔE_f) for the addition of a hetero-M atom onto a Ru SAC [a negative (exothermic) ΔE_f value means the stable formation of hetero-RuM DACs from Ru SACs, and *vice versa*] as follows:

$$\Delta E_f(\text{RuM/C}) = E(\text{RuM/C}) - [E(\text{Ru/C}) + E(\text{M})]$$

where E(RuM/C), E(Ru/C), and E(M) represent the total energy of the RuM/C surface, the bare Ru_1 SAC surface, and an isolated M atom, respectively. Here, the choice of an isolated M atom for ΔE_f is based on the synthesis method of single or double atom catalysts, where atomic layer deposition or sputtering has been used for the utilization of atoms.[46,69–71]

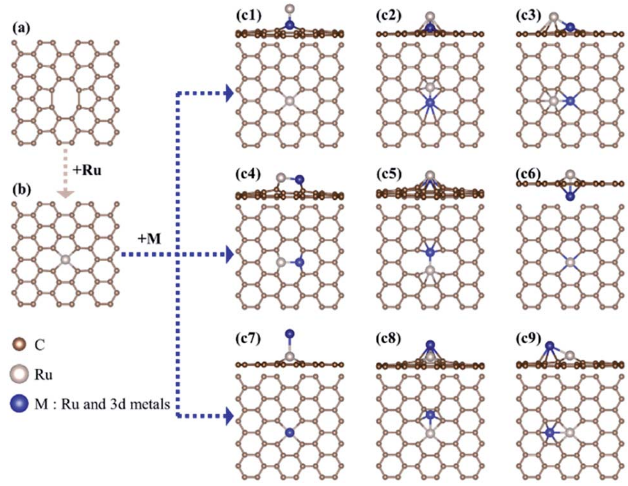

Fig. 4 A schematic diagram and possible geometries for RuM/C catalysts.

Here, to find the most stable geometric ensemble of hetero-RuM DACs, we compare the calculated ΔE_f values of nine possible ensemble geometries (referred to as *c*1, *c*2, *c*3, *c*4, *c*5, *c*6, *c*7, *c*8, and *c*9) (see Fig. 4 and Table 1). For the comparison, the homo-Ru_2 DAC case is also presented. We see that the most stable geometric ensemble of the RuM/C system is classified into three groups. That is, (1) group I (*c*4 geometry) (we call horizontal double atom); the Ru–M dimer [M = Ru ($\Delta E_f = -3.69$ eV), Ti ($\Delta E_f = -4.49$ eV), V ($\Delta E_f = -3.96$ eV), and Cr ($\Delta E_f = -1.72$ eV)] is nearly horizontally adsorbed at two carbon vacant sites, leading to chemical bond formation between a Ru (or M) atom and two C atoms and (2) group II (*c*8 geometry) (we call inclined pentagon M double atom); the Ru–M dimer [M = Sc ($\Delta E_f = -4.23$ eV), Mn ($\Delta E_f = -1.82$ eV), and Fe ($\Delta E_f = -2.41$ eV)] are connected to one carbon vacant and hollow carbon sites. Here, Ru and M atoms are associated with rectangular- and pentagonal-shaped four carbons, respectively, leading to the formation of an inclined RuM structure. (3) Group III (*c*9 geometry) (we call inclined hexagon M double atom); the configuration of the Ru–M dimer [M = Co ($\Delta E_f = -2.49$ eV) and Ni ($\Delta E_f = -2.87$ eV)] is similar to that in the group II case, except that M atoms are bound to hexagon-shaped five carbons, respectively. Here, group III also shows an inclined RuM structure. The optimized ensemble geometries of all hetero-Ru DACs are shown in Fig. S2.† In the following section, we investigate the electrocatalytic activity of hetero-RuM DACs toward NH_3 formation in the most stable models.

Reactivity of hetero-RuM double atom catalysts

Fig. 5 shows the calculated ΔG_{diss} for the $N_2(g) \rightarrow N^* + N^*$ reaction on the surface of the hetero-RuM DACs. We observe the endothermic process when M is Ti, V, Cr, and Fe in RuM/C [note that $\Delta G_{diss} = 1.29$ eV (Ti), $\Delta G_{diss} = 0.85$ eV (V), $\Delta G_{diss} = 0.58$ eV (Cr), and $\Delta G_{diss} = 0.07$ eV (Fe)], suggesting that the N_2RR *via* the dissociative mechanism is energetically unfavourable. On the other hand, the RuSc/C, RuMn/C, RuCo/C, and RuNi/C cases

Table 1 Calculated formation energy (ΔE_f/eV) of RuM according to various geometries. In this table, the bold text indicates the formation energy of the most stable geometry

	*c*1	*c*2	*c*3	*c*4	*c*5	*c*6	*c*7	*c*8	*c*9
Ru_2/C	−2.98	−3.22	−3.39	**−3.69**	−2.02	−3.23	—	—	—
RuTi/C	1.09	—	—	−2.58	−1.30	−4.14	−2.74	**−4.23**	−4.13
RuV/C	−0.92	−2.83	—	**−4.49**	−2.52	−4.04	−2.90	−4.42	−4.23
RuCr/C	−1.78	−2.97	−2.55	**−3.96**	−1.99	−2.93	−2.16	−3.09	−3.19
RuSc/C	−0.39	−1.07	−0.79	**−1.72**	−0.03	−1.27	−1.04	−1.46	−1.37
RuMn/C	−0.28	−0.98	−0.94	−1.75	0.20	−1.45	−1.20	**−1.82**	−1.71
RuFe/C	−0.90	−1.74	−1.64	−2.26	−0.71	−1.81	−1.83	**−2.41**	−2.35
RuCo/C	−0.80	−1.97	−2.36	−2.31	−0.56	−2.00	−1.91	−2.40	**−2.49**
RuNi/C	—	−2.16	−2.00	−2.15	—	−2.48	−2.51	−2.73	**−2.87**

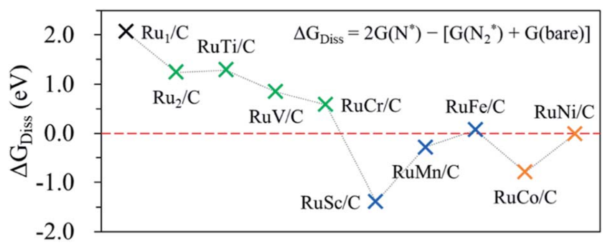

Fig. 5 Calculated N_2 dissociation energy (ΔG_{diss}) to determine the reaction mechanism.

exhibit negative ΔG_{diss} values [−1.39 eV (Sc), −0.28 eV (Mn), −0.79 eV (Co), and −0.01 eV (Ni)], indicating that there is a possibility for the dissociative N_2RR on those catalysts. Even if the ΔG_{diss} value is less than zero, the dissociative NRR will not occur if the barrier (ΔG_{barr}) is insurmountably high under the reaction conditions. The ΔG_{diss} value on the stepped Ru (0001) surface, which is known to be capable of the dissociative N_2RR under standard temperature and pressure conditions, is 0.78 eV.[21,72] Zhao *et al.* reported that they did not consider the dissociative N_2RR because the dissociation barrier of N_2* in their catalyst (Mo SAC on BN) was as high as 4.25 eV.[40] To clearly determine which mechanism to follow on hetero-RuM/C, we calculate ΔG_{barr} for the RuSc/C, RuMn/C, and RuCo/C catalysts with substantial negative values of ΔG_{diss}, as well as for the RuNi/C and RuFe/C catalysts with near zero values of ΔG_{diss} (see Fig. S3†). We find that all the ΔG_{barr} values are above 2.2 eV [note that ΔG_{barr}(Sc), ΔG_{barr}(Mn), ΔG_{barr}(Fe), ΔG_{barr}(Co), and ΔG_{barr}(Ni) are 2.92 eV, 2.43 eV, 2.71 eV, 2.40 eV, and 2.22 eV, respectively], suggesting that the N_2RR *via* the dissociative mechanism cannot occur on the RuSc/C, RuMn/C, RuCo/C, RuNi/C and RuFe/C surfaces under the reaction conditions.

Fig. 6 displays the Gibbs free energy diagram for the favourable pathway for the N_2RR on the hetero-RuM DACs. The PLS for the N_2RR on the Ru_1 SAC and homo-Ru_2 DAC is the protonation of N_2* to form N_2H* (see Fig. 3). However, in the case of hetero-RuM DACs, the PLS is changed to the protonation of NH_2* except for hetero-RuFe and RuTi DACs. We also find that the onset potential for NH_3 formation strongly depends on the type of M, and hetero-RuM DACs show a less negative onset potential than the Ru_1 SAC (−1.14 V) except for the hetero-RuV DAC. In particular, the hetero-RuSc, RuMn, and RuFe in group II (inclined pentagon M double atom) have a less negative onset potential [−0.89 V (RuSc/C), −0.81 V (RuMn/C), and −0.73 V (RuFe/C), where RuFe exhibits the best activity toward NH_3 production] than the homo-Ru_2 DAC [−0.91 V], indicating a reduced over-potential and in turn enhanced NH_3 productivity for the hetero-RuSc, RuMn, and RuFe DACs. In contrast, for the hetero-RuTi, RuV, and RuCr DACs in group I (horizontal double atom) [−1.12 V (RuTi/C), −1.27 V (RuV/C), and −1.06 V (RuCr/C)], and RuCo and RuNi DACs in group III (inclined hexagon M double atom) [−1.02 V (RuCo/C) and −1.06 V (RuNi/C)], the opposite is true.

Next, we display the change of the onset potentials of the Ru_1 SAC, homo-Ru DAC, and hetero-RuM DACs for NH_3 production as a function of the adsorption energy of N_2H and NH_2 (see Fig. 7). The calculated $\Delta E_{ads}(N_2H)$ and $\Delta E_{ads}(NH_2)$ are summarized in Table S2.†

We see a clear volcanic relationship between the onset potential of the N_2RR and $\Delta E_{ads}(NH_2)$, whereas there is no correlation between the onset potential and $\Delta E_{ads}(N_2H)$. The strong dependence of N_2RR activity in the RuM system on $\Delta E_{ads}(NH_2)$ [rather than $\Delta E_{ads}(N_2H)$] is related to the PLS we have identified. For most RuM (M = V, Cr, Sc, Mn, Co, Ni) cases, the PLS is NH_2* protonation [(4) $NH_2^* + (H^+ + e^-) \rightarrow NH_3(g)$], where the level of $\Delta E_{ads}(NH_2)$ determines the reactivity toward NH_3 production. That is, the strong binding of NH_2 to the catalyst leads to a decrease in reaction potential and *vice versa*. Thus, $\Delta E_{ads}(NH_2)$ can be used for the representation of NH_3 productivity *via* the N_2RR, which is called as the descriptor.

Looking closely at the volcano plot of Fig. 7(b), the lowering of the descriptor values [$\Delta E_{ads}(NH_2)$] compared to the Ru_1 SAC increases the activity (onset potential) of hetero-RuM DACs (M = Ru, Ti, and Fe) toward NH_3 production until the $\Delta E_{ads}(NH_2)$ value approaches about −3.68 eV (which is defined as the peak position of the volcanic activity-descriptor plot). After that, the N_2RR activity is reduced (onset potential is lowered) as descriptor values are further lowered. Here, the opposition correlation between the right and left sides of the volcano plot is related to the type of PLS. On the left leg of the volcano plot, the PLS is the protonation of NH_2* [(5) $NH_2^* + (H^+ + e^-) \rightarrow NH_3(g)$] regardless of its mechanism, where the level of NH_2 adsorption energy (descriptor value) determines the reactivity toward NH_3 production. That is, the strong binding of NH_2 to the catalyst leads to a decrease in the reaction potential. On the other hand,

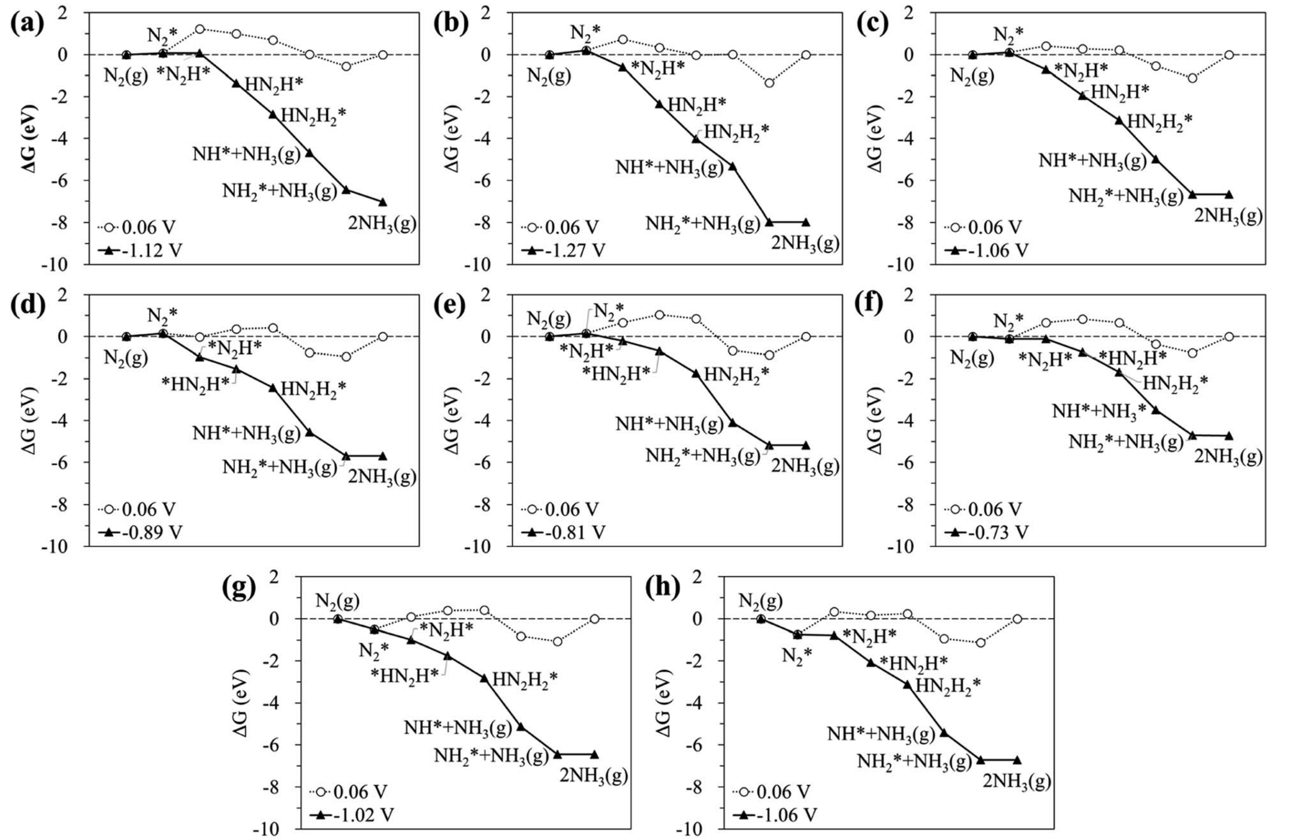

Fig. 6 Calculated Gibbs free energy profiles at equilibrium (○) and limiting (▲) potentials for the N_2RR on hetero-RuM DACs of group I [((a) RuTi/C, (b) RuV/C, and (c) RuCr/V)], group II [(d) (RuSc/C, (e) RuMn/C, and (f) RuFe/C)], and group III [(g) RuCo/C and (h) RuNi/C] *via* the most favourable pathway.

on the right leg of the volcano plot, the N_2RR occurs *via* the associative mechanism due to the weak ability to bind the reaction intermediates such as NH_2, where the increase of NH_2 affinity enhances the NH_3 productivity.

Origin of the enhanced N_2RR catalysis for hetero-RuM double atom catalysts

Decoupling strain, dopant and configurational effects. The reactivity of hetero-RuM DACs compared to the homo-Ru_2 DAC can be modified by three factors. The first one is related to the atomic size mismatch in the Ru–M system. In bimetallic catalysis, the lattice distance of the bulk metal determines the d-band structure and in turn the surface reactivity.[72–74] Thus, the atomic distance between Ru and M is one of the most important factors in determining the activity of the catalyst, which is called as the strain effect. The second one is the change of catalytic activity in both Ru and M atoms induced by the interatomic mixing between hetero-Ru and M atoms.[75,76] That is, compared to the respective pure Ru and M atoms, the d-band structures of both Ru and M atoms in hetero-RuM DACs are significantly changed by the electronic charge transfer between Ru and M atoms and in turn affects the binding energy of reaction intermediates on hetero-RuM DACs, which is referred to as the dopant effect. The last configurational effect is the modification of catalytic activity caused by the structural change of RuM DACs by the strong interaction between the hetero-RuM double atom and the graphene. That is, the configurational effect induces the geometric ensemble configuration change of the hetero-RuM DACs from the horizontal Ru_2 DAC to the inclined pentagon M double atom, which affects the binding energy of reaction intermediates in the N_2RR.

To clearly understand the relative role of strain, dopant and configurational effects in determining NH_3 productivity in the hetero-RuM DACs in group II catalysts (here, we choose group II catalysts which exhibit higher N_2RR activity compared to the group I and III cases), we decoupled these three effects as shown in Fig. 8 and Table S3.† We also displayed optimized N_2-, N_2H-, and NH_2-adsorbed geometries in Fig. S4.†

First, we attempt to only extract the strain effect from the total N_2RR catalysis by calculating the onset potential for strained homo-Ru_2 DACs having the same geometric configuration as the homo-Ru_2 DAC but having a different Ru–Ru bond distance (indicated by $RuM_{strained}$). To model $RuM_{strained}$, we use the optimized atomic position from hetero-RuM DACs with the geometry of horizontal double atom (group I). Compared to the homo-Ru_2 DAC case (2.276 Å), the Ru–Ru bond distance for the $RuSc_{strained}$, $RuMn_{strained}$, and $RuFe_{strained}$ models is 2.300, 2.135 and 2.142 Å, respectively, which are under a tensile strain of +1.05% and compressive strain of −6.20% and −5.90%, respectively, (note that '+' and '−' signs represent the tensile

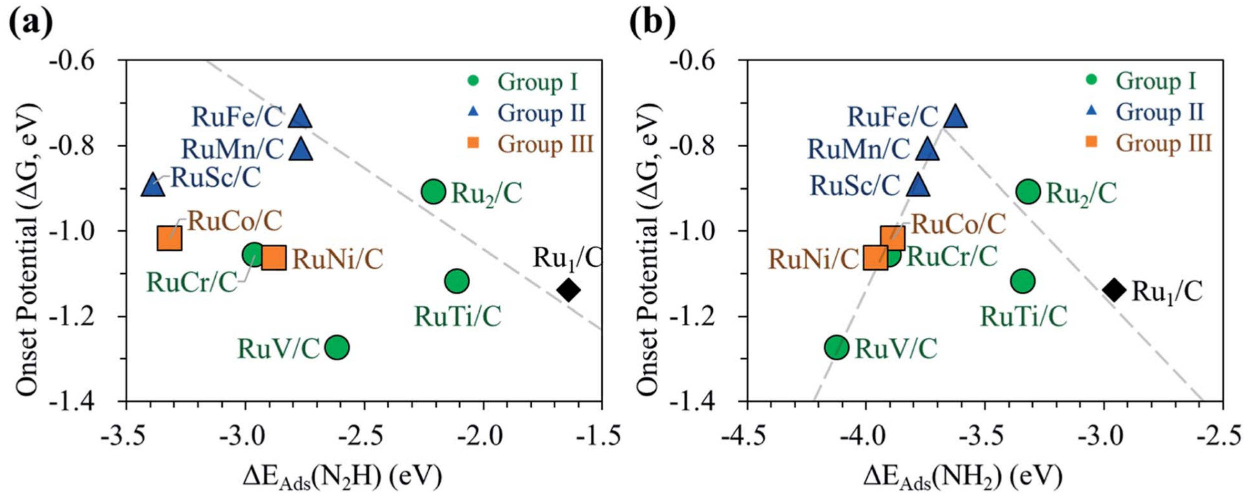

Fig. 7 Relationship between the onset potential of the N_2RR and the adsorption energies of (a) N_2H and (b) NH_2. In (b), the PLS of the catalysts located on the left side of the peak position is (5) $NH_2^* + (H^+ + e^-) \rightarrow NH_3(g)$, while for the right-side case, the PLS is (6) $N_2^* + (H^+ + e^-) \rightarrow N_2H^*$.

and compressive strain, respectively). Our DFT calculation predicts a substantial decrease of onset potential by 0.15 V for the $RuSc_{strained}$ catalyst, but a small variation for the $RuFe_{strained}$ (onset potential decreases by 0.05 V) and $RuMn_{strained}$ (onset potential decreases by ~0 V) catalysts [see Fig. 8(a)], suggesting that the tensile strain tends to reduce the NH_3 productivity *via* the N_2RR, while the effect of compressive strain is insignificant. The large decrease of onset potential in the $RuSc_{strained}$ catalyst is related to the decrease of N_2 adsorption energy (increase of N_2 affinity) [see Fig. 8(b)] from −0.84 V (homo-Ru_2 DAC) to −1.10 V and little change of N_2H adsorption energy [see Fig. 8(c)], which only raise the level of reactant energy for the potential limiting step [(6) $N_2^* + (H^+ + e^-) \rightarrow N_2H^*$] and in turn increase the endothermicity of the reaction.

Next, for the calculation of the contribution of the dopant effect to the NH_3 formation, we prepared $RuSc_{doped}$, $RuMn_{doped}$,

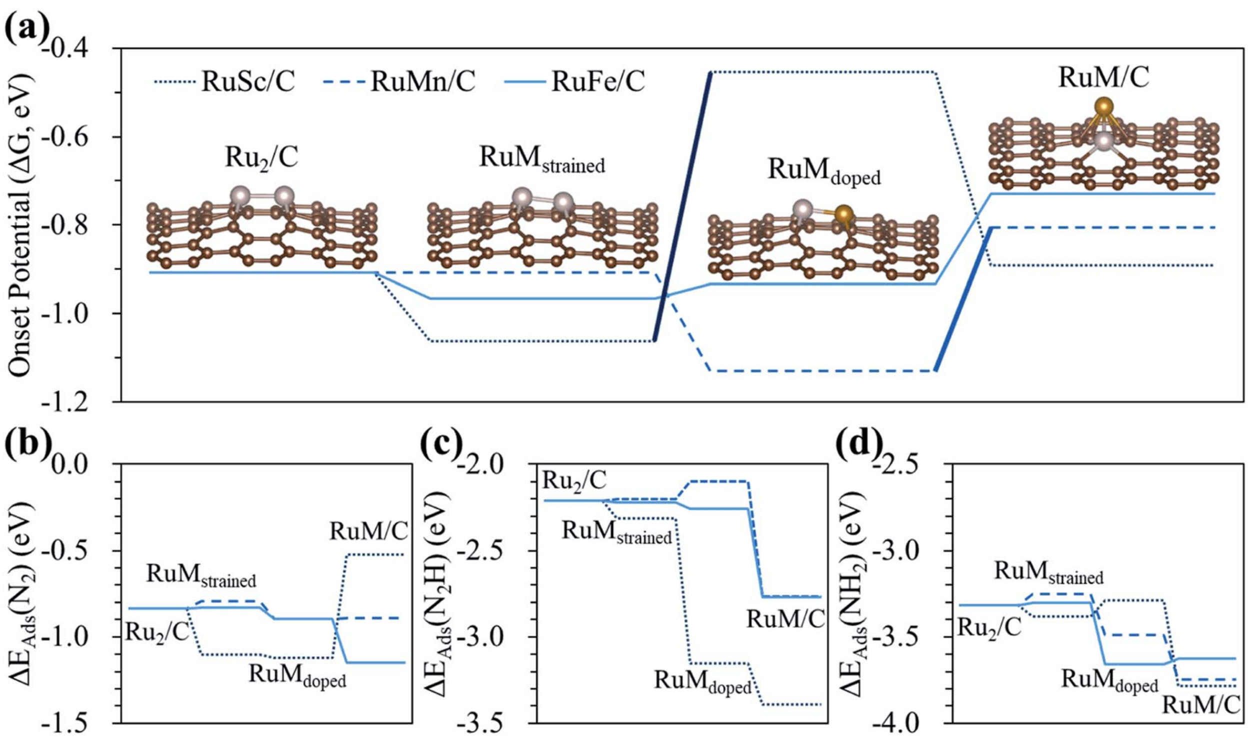

Fig. 8 Contribution of strain, dopant and configurational effects to the (a) onset potential, and adsorption energy of (b) N_2, (c) N_2H, and (d) NH_2 of the N_2RR on the hetero-RuM DACs. In (a), the bold solid lines indicate the change in the limiting step from [$N_2^* + (H^+ + e^-) \rightarrow N_2H^*$] to [$NH_2^* + (H^+ + e^-) \rightarrow NH_3(g)$].

and $RuFe_{doped}$ models by replacing a Ru atom by a Sc, Mn, and Fe atom in $RuSc_{strained}$, $RuMn_{strained}$, and $RuFe_{strained}$ models, respectively. Here, the change of onset potential from the $RuM_{strained}$ model to the RuM_{doped} model indicates the contribution of the dopant effect to total catalysis. We find different aspects for all three catalysts due to the dopant effect. For the $RuSc_{doped}$ case, the onset potential is significantly increased to −0.45 V compared to the $RuSc_{strained}$ model, which is related to the dramatic increase of N_2H affinity [$\Delta E_{ads}(N_2H) = -3.15$ eV] and almost no change of N_2 binding energy [$\Delta E_{ads}(N_2) = -1.12$ eV] compared to the $RuSc_{strained}$ model [$\Delta E_{ads}(N_2H) = -2.31$ eV and $\Delta E_{ads}(N_2) = -1.10$ eV] [see Fig. 8(b) and (c)]. Consequently, this induces the shift of the PLS from [(6) $N_2* + (H^+ + e^-) \rightarrow N_2H*$] to [(5) $NH_2* + (H^+ + e^-) \rightarrow NH_3(g)$]. In the case of $RuMn_{doped}$, the onset potential is decreased to −1.13 V by the dopant effect compared to the $RuMn_{strained}$ model. Unlike the $RuSc_{doped}$ case, this is mainly connected to the stronger N_2 adsorption and weaker N_2H adsorption [$\Delta E_{ads}(N_2) = -0.90$ eV and $\Delta E_{ads}(N_2H) = -2.10$ eV]. However, the N_2RR onset potential (−0.93 V) and the adsorption energies of N_2 [$\Delta E_{ads}(N_2) = -0.90$ eV] and N_2H [$\Delta E_{ads}(N_2H) = -2.26$ eV] on the $RuFe_{doped}$ model are changed little by the dopant effect compared to the $RuFe_{strained}$ models [−0.96 V (onset potential), $\Delta E_{ads}(N_2) = -0.83$ eV] and [$\Delta E_{ads}(N_2H) = -2.22$ eV].

For the contribution of the configurational effect to the total N_2RR catalysis, we calculate the difference of the onset potentials between the RuM_{doped} models and hetero-RuM DACs. Notice that the configurational effect induces the geometric ensemble configuration change of the hetero-RuSc, RuMn, and RuFe DACs from group I (horizontal double atom) to group II (inclined pentagon M double atom), which affects the N_2RR catalysis. We find that for the hetero-RuSc DAC, the N_2RR activity (onset potential) is reduced by 0.44 V since the NH_2 adsorption energy is decreased from −3.29 eV to −3.78 eV by the configurational effect. For the RuMn and RuFe DAC cases, the onset potential is increased from −1.13 V and −0.93 V to −0.81 V and −0.73 V, respectively, which is related to the increase of N_2H affinity by 0.67 eV and 0.51 eV compared to the respective $RuMn_{doped}$ and $RuFe_{doped}$ models. Especially for the RuMn case, the potential limiting step is shifted to (5) $NH_2* + (H^+ + e^-) \rightarrow NH_3(g)$ due to the strong NH_2 adsorption. These results demonstrate that the strain, dopant and configurational effects play an important role in determining NH_3 productivity *via* electrochemical N_2 reduction. In particular, the dopant and configurational effects are responsible for the enhancement of NH_3 production.

Electronic structure analysis. To better understand the fundamental reason why the hetero-RuM DACs boost the NH_3 production compared to the homo-Ru_2 DAC, we calculate the d-

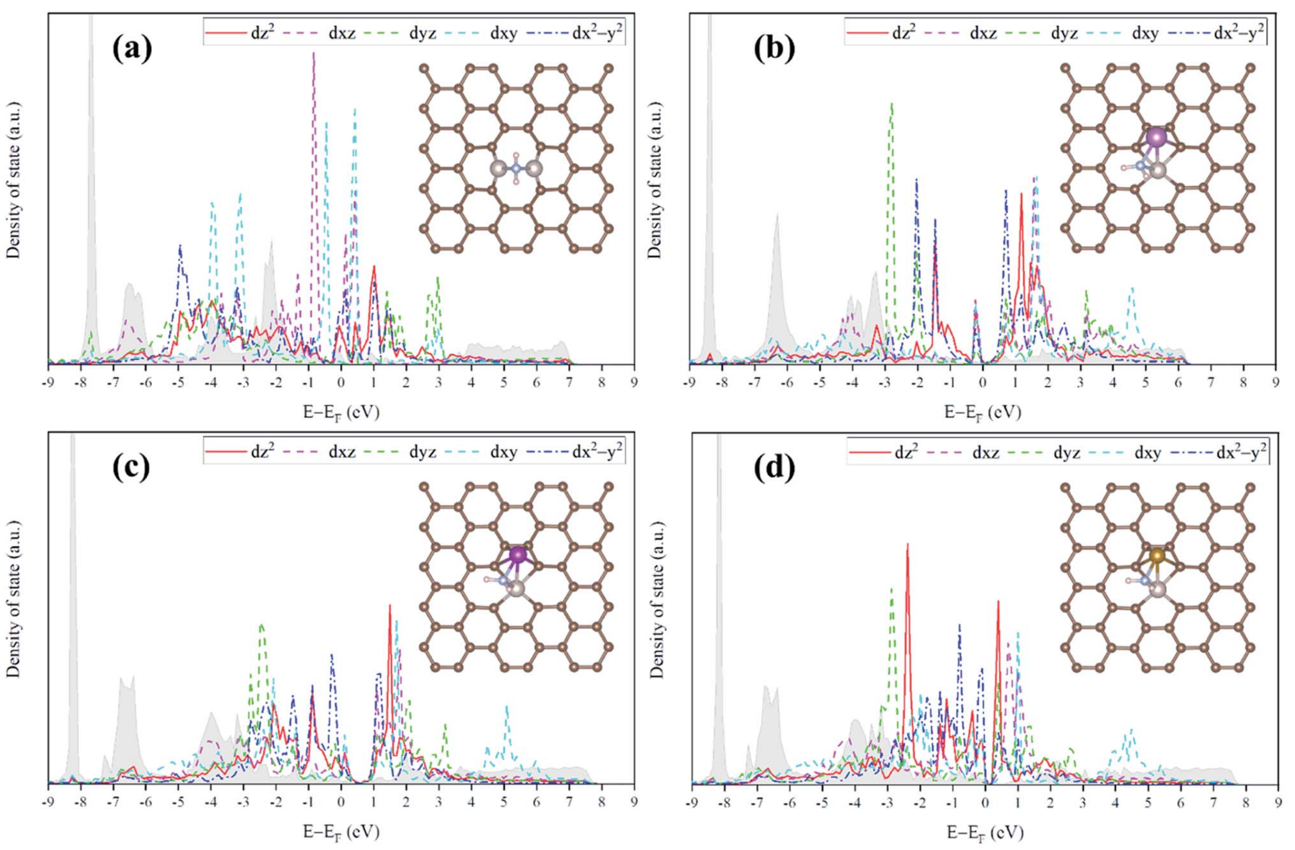

Fig. 9 Average d-orbital resolved density of states (ORDOS) (d_{z^2}, d_{xz}, d_{yz}, d_{xy}, and $d_{x^2-y^2}$) of the Ru/M atoms and the p-density of states (DOS) of the N atom in NH_2 (descriptor for representing the NH_3 production catalysis) for the NH_2-adsorbed (a) homo-Ru_2 DAC, and (b) hetero-RuSc, (c) hetero-RuMn, and (d) hetero-RuFe DACs. The DOS for the p orbital of N in NH_2 is shown as the grey area.

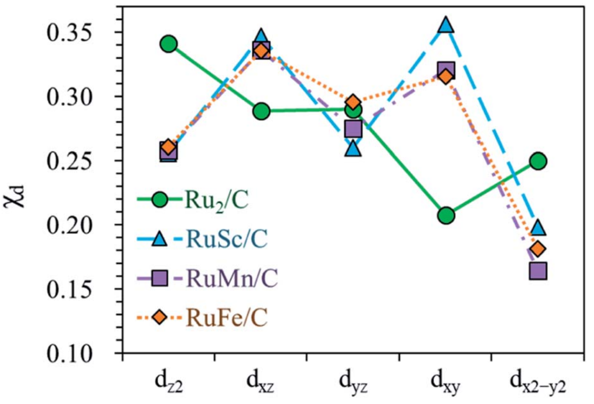

Fig. 10 Fraction of p–d orbital overlap in the total p orbital of the N atom (indicated by χ_d) according to the variation of the type of d orbital (d_{z^2}, d_{xz}, d_{yz}, d_{xy}, and $d_{x^2-y^2}$).

orbital resolved density of states (ORDOS) (d_{z^2}, d_{xz}, d_{yz}, d_{xy}, and $d_{x^2-y^2}$) of the Ru and M (M = Sc, Mn, Fe) atoms and the p density of states (DOS) of the N atom in the NH_2 for the NH_2-adsorbed homo-Ru_2 and hetero-RuM DACs [see Fig. 9]. Here, the introduction of a hetero-M atom into the homo-Ru_2 atom can affect the electronic structure of the catalyst through dopant and configurational effects and in turn modify the binding energy of the descriptor NH_2 for representing the NH_3 production catalysis. Thus, it is worthwhile to comprehend the change of the electronic structure induced by the-hereto M atom for the rational design of catalysts.

For the homo-Ru_2 DAC case, we see strong interatomic mixing between the p orbital of N in adsorbed NH_2 and the d_{z^2}, d_{xz}, d_{yz}, d_{xy}, and $d_{x^2-y^2}$ orbitals of Ru_2 DAC in the energy ranges from −7.0 eV to −6.0 eV, from −4.5 eV to −3.5 eV and from −3.0 eV to −1.5 eV. To quantitatively understand the degree of interatomic mixing between each d orbital and p orbital, we calculate the fraction of p–d orbital overlap in the total p orbital of the N atom (referred to as χ_d) (see Fig. 10). Our DFT calculation shows that the order of overlap between p and d orbitals is d_{z^2} ($\chi_{d_{z^2}} = 0.341$) > d_{xz} ($\chi_{d_{xz}} = 0.289$), d_{yz} ($\chi_{d_{yz}} = 0.290$) > $d_{x^2-y^2}$ ($\chi_{d_{x^2-y^2}} = 0.250$) > d_{xy} ($\chi_{d_{xy}} = 0.208$). This suggests that the orbitals (d_{z^2}, d_{xz}, and d_{yz}) having an orientation toward the z direction in the Ru_2 double atom [which is horizontally placed in the x–y plane; group I] have a higher impact in determining the adsorption of NH_2 with the catalyst than $d_{x^2-y^2}$ and d_{xy}.

On the other hand, for the hetero-RuFe DAC case, we find a strong overlap between the p orbital and d orbitals in the range from −4.5 eV to −2.5 eV (see Fig. 9(d)). In particular, unlike the homo-Ru_2 DAC case (key orbitals in bonding are in the order of d_{z^2} > d_{xz} > d_{yz}), the d_{xz} and d_{xy} orbitals exhibit larger interatomic mixing with p orbital cases, suggesting that the orbitals (d_{xz} and d_{xy}) having an orientation toward the x direction play an important role in stabilizing a NH_2 adsorbate on the hetero-RuFe DAC. Note that d_{xz} ($\chi_{d_{xz}} = 0.336$) > d_{xy} ($\chi_{d_{xy}} = 0.315$) > d_{yz} ($\chi_{d_{yz}} = 0.296$) > d_{z^2} ($\chi_{d_{z^2}} = 0.261$) > $d_{x^2-y^2}$ ($\chi_{d_{x^2-y^2}} = 0.182$) (see Fig. 10). Here, the different nature of p–d orbital overlap between the homo-Ru_2 DAC and hetero-RuFe DAC is related to the geometric ensemble difference of double atoms induced by the strong hetero-dopant-support effect. That is, unlike the homo-Ru_2 DAC [whose two atoms are horizontally placed in the x direction; group I (horizontal double atom)], the hetero-RuFe DAC [group II (inclined pentagon M double atom)] has an inclined geometric ensemble structure in the y-direction where each Ru and M atom has a different z position in the normal direction of the x–y plane (see Fig. S2†). This makes the d_{xz} and d_{xy} orbitals more favourable for the interaction with the p orbital of NH_2 than the d_{z^2}, $d_{x^2-y^2}$ and d_{yz} orbitals, leading to the tilted adsorption configuration of NH_2 on the RuFe DAC. For the RuSc and RuMn DACs, we see a similar p–d orbital overlap to the RuFe case, that is, the p orbital mixing mainly with d_{xz} and d_{xy} in the range from −5.0 eV to −2.7 eV (from −7.0 eV to

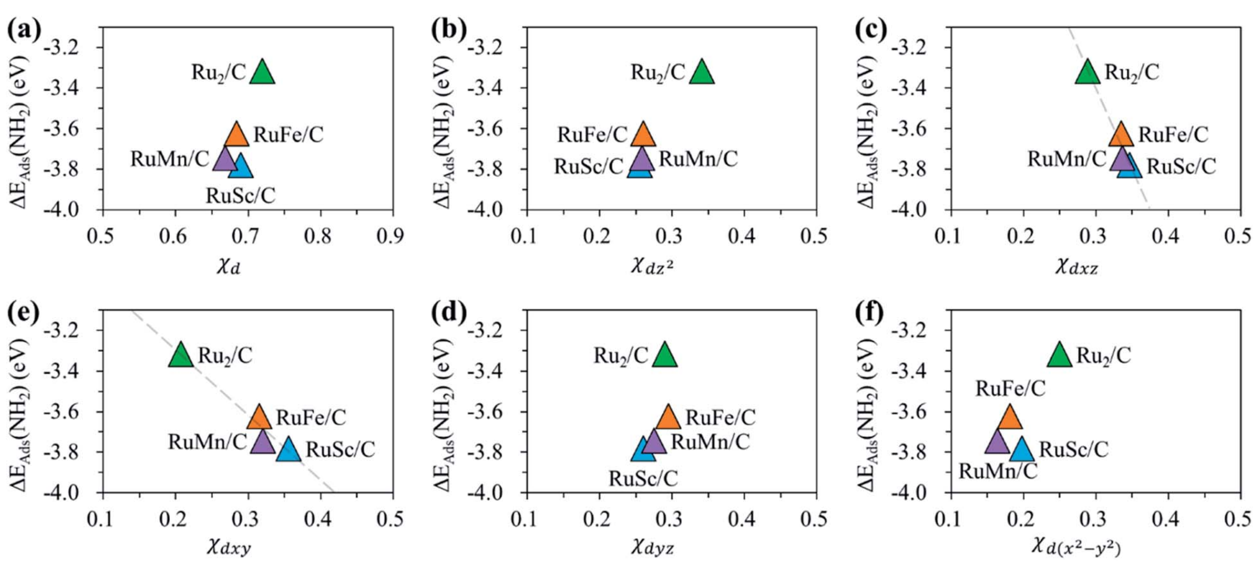

Fig. 11 Relationship between NH_2 adsorption energy [$\Delta E_{ads}(NH_2)$] and orbital overlap [χ_d] for the RuM (M = Sc, Mn, Fe) DACs (a) χ_d, (b) $\chi_{d_{z^2}}$, (c) $\chi_{d_{xz}}$, (d) $\chi_{d_{yz}}$, (e) $\chi_{d_{xy}}$ and (f) $\chi_{d_{x^2-y^2}}$.

Table 2 Difference between the onset potential of the N_2RR and HER on the Ru SAC, and homo- and hetero-RuM DACs. Units are given in V

		Group I				Group II			Group III	
	Ru_1/C	Ru_2/C	RuTi/C	RuV/C	RuCr/C	RuSc/C	RuMn/C	RuFe/C	RuCo/C	RuNi/C
ΔG_{NRR}	−1.14	−0.91	−1.12	−1.27	−1.06	−0.89	−0.81	−0.73	−1.02	−1.06
ΔG_{HER}	−0.22	−0.37	−0.20	−0.77	−0.55	−0.36	−0.29	−0.42	−0.81	−0.80
$\Delta\Delta G$	−0.91	−0.54	−0.92	−0.51	−0.51	−0.53	−0.52	−0.31	−0.21	−0.26

−6.0 eV) for the RuSc DAC and from −4.7 eV to −2.6 eV for RuMn DAC. This demonstrates that the dopant and configurational effects in a hetero-RuM double atom induce an inclined RuM geometric ensemble configuration and in turn activate the d_{xz} and d_{xy} orbitals for NH_2 adsorption (rather than the d_{z^2} and $d_{xy} + d_{x^2-y^2}$ orbitals), leading to the modification of NH_2 binding energy.

Fig. 11 shows the relationship between $\Delta E_{ads}(NH_2)$ and χ_d for the RuM (M = Sc, Mn, Fe) DACs. We find that for the d_{xz} and d_{xy} orbitals, the increase of p–d orbital overlap (χ_d) enhances the NH_2 affinity linearly, while for the d_{z^2}, $d_{x^2-y^2}$ and d_{yz} orbitals, no clear relationship is observed. This indicates that the d_{xz} and d_{xy} orbitals have a higher impact in determining the NH_2 adsorption process, which is in line with the larger p–d overlap of the d_{xz} and d_{xy} orbitals than the d_{z^2}, $d_{x^2-y^2}$ and d_{yz} orbitals as discussed above.

HER activity

In addition to the N_2RR studies on the RuM DACs, we calculate the onset potential of the hydrogen evolution reaction (HER),

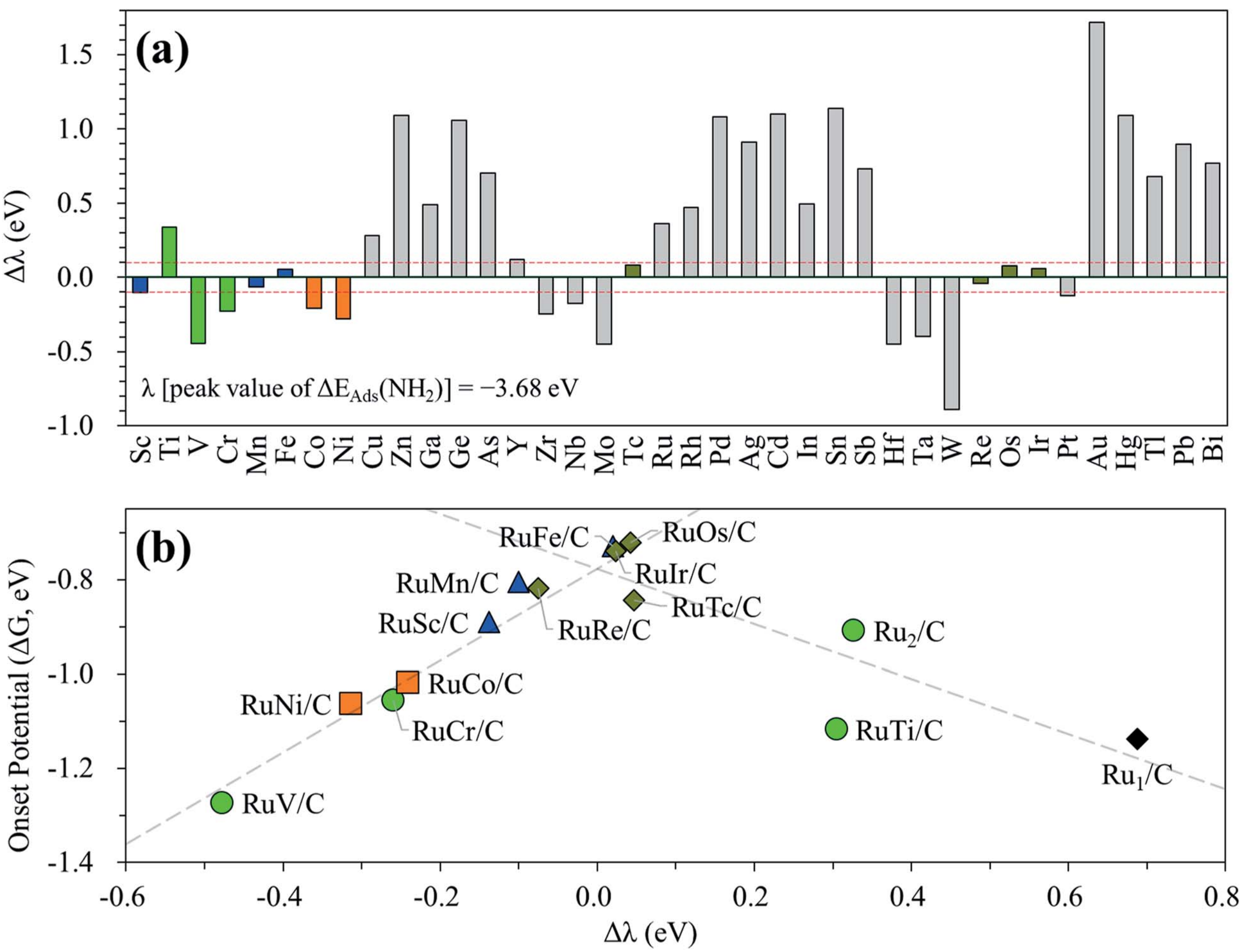

Fig. 12 (a) Screening results using NH_2 adsorption energy as a descriptor in RuM/C, in which M is extended to 4d, 5d, 5p, and 6p elements, and (b) revised volcano plot by adding four more candidates. In (b), the PLS of the catalysts located on the left leg of the peak position is [(5) $NH_2^* + (H^+ + e^-) \rightarrow NH_3(g)$], while for the right leg case, the PLS is [(6) $N_2^* + (H^+ + e^-) \rightarrow N_2H^*$].

which is one of the reasons for lowering the faradaic efficiency of NH_3 production.[13,42,45] The calculated onset potentials of the N_2RR (ΔG_{NRR}) and HER (ΔG_{HER}) and the difference of onset potentials between the N_2RR and HER (indicated by $\Delta\Delta G = \Delta G_{NRR} - \Delta G_{HER}$) on the Ru_1 SAC, homo-Ru_2 DAC, and hetero-DACs are shown in Table 2. Our DFT calculation shows the enhanced selectivity ($\Delta\Delta G = -0.31$ eV) of the most active hetero-ReFe double atom catalyst toward the N_2RR over the HER compared to the Ru_1 SAC ($\Delta\Delta G = -0.91$ eV) and homo-Ru DAC ($\Delta\Delta G = -0.54$ eV) cases. However, the onset potentials of the N_2RR for all RuM catalysts are still lower than the HER onset potential.

Screening for additional hetero-RuM double atom catalysts

In the above investigation of the hetero-RuM DACs (whose M is a 3d transition metal) for NH_3 production, we concluded that a hetero-RuFe DAC is the best catalyst. To find out if there is a catalyst with better activity than a hetero-RuFe DAC, we further screen the candidate materials by engineering the chemical composition of RuM (M = 4d, 5d, and p blocks) using the descriptor (which is NH_2 adsorption energy and is indicated by λ) to predict the onset potential. First, the most stable geometry of the expanded hetero-RuM DACs was investigated using the same procedure as that in the case of 3d transition metals, and these results are shown in Table S4.† Using this optimized hetero-RuM DAC geometry, we further calculated the adsorption energy of NH_2, the descriptor for N_2RR activity we found. Fig. 12(a) displays the relative descriptor (denoted as $\Delta\lambda$) compared to the descriptor value of the peak position in the volcano plot ($\lambda = -3.68$ eV) identified in the above section (see Fig. 7(b)). We find that the descriptor value depends on the chemical composition and tends to increase as M moves to the right of the periodic table in the hetero-RuM DACs. Here, based on $-0.1 \text{ eV} < \Delta\lambda < 0.1$ eV, we select four candidates (hetero-RuTc, RuRe, RuOs, and RuIr DACs), which can be expected to enhance NH_3 production *via* electrochemical N_2 reduction. The calculated onset potentials for these candidates are shown in Fig. 12(b). We see a higher NH_3 production reactivity (in particular, hetero-RuOs and RuIr DACs, whose onset potentials are -0.72 V and -0.74 V, respectively) than that of the homo-Ru_2 DAC case (-0.91 V), which is close to the onset potential of the hetero-RuFe DAC (-0.73 V).

We also calculate the onset potentials of the HER (ΔG_{HER}) on the additional four candidates and compared with the onset potential of the N_2RR (ΔG_{NRR}) to evaluate N_2RR selectivity (see Table S5†). However, ΔG_{HER} on all those candidates is also lower than ΔG_{NRR}. Improving the selectivity by increasing the N_2RR onset potential over the HER remains one of the biggest challenges to be addressed in the subsequent study.

Conclusions

In this study, using spin-polarized DFT calculations, we investigated NH_3 production catalysis *via* the electrochemical N_2 reduction (N_2RR) on hetero-RuM (M = 3d transition metal) double atom catalysts supported on defective graphene and computationally screened novel catalysts by exploring 4d, 5d and p block metals as the hetero-M metals.

First, we investigated the geometric ensemble structure of the hetero-RuM double atom catalysts on carbon vacant graphene. Depending on the type of hetero-atom, we identified three possible ensemble configurations; (1) group I: the horizontal double atom (Ru_2, RuTi, RuV, and RuCr), (2) group II: the inclined pentagon M double atom (RuSc, RuMn, and RuFe), and (3) group III: the inclined hexagon M double atom (RuCo and RuNi).

Second, our DFT calculation predicted the significantly enhanced N_2RR activity (reduced over-potential) of the inclined pentagon M double atom catalysts (group II) (such as RuFe, RuMn, and RuSc) (RuFe has the highest activity) compared to the homo-Ru_2 double atom case. By looking at the potential limiting step, we found that the NH_2 binding energy (so-called descriptor) was suitable for representing the N_2RR onset potential on the hetero-RuM double atom catalyst. In addition, from the volcanic activity-descriptor plot, we found that the peak position for a descriptor was around about -3.68 eV. We further searched for the catalyst candidate using the descriptor to represent onset potential by varying the chemical composition of RuM (M = 4d, 5d, and p blocks), which leads to the discovery of promising hetero-RuOs and RuIr double atom catalysts, whose onset potentials were close to the onset potential of the hetero-RuFe catalyst.

Third, the study on the relative role of strain, dopant and configurational effects in the inclined pentagon M double atom catalysts (RuFe, RuMn, and RuSc) demonstrated that the strain, dopant and configurational effects play an important role in determining NH_3 productivity *via* electrochemical N_2 reduction. That is, (1) the tensile strain (RuSc) tended to reduce the NH_3 productivity *via* the N_2RR, while the effect of compressive strain (RuFe and RuMn) was insignificant, (2) the dopant effect was found to have a significant effect on N_2RR activity, that is, a beneficial effect for the RuSc and RuFe cases and a detrimental effect for the RuMn case, and (3) the dopant-support interaction induced the change of the ensemble structure from the horizontal double atom to the inclined pentagon M double atom, where the N_2RR activity on the RuSc double atoms was substantially reduced, while for the RuFe, and RuMn cases, the change in the ensemble structure resulted in the enhancement of N_2RR activity.

Finally, our DFT calculation for the analysis of the p–d (d_{z^2}, d_{xz}, d_{yz}, d_{xy}, and $d_{x^2-y^2}$) orbital overlap identified the key d orbitals in determining the affinity of the descriptor NH_2. That is, the orbitals (d_{z^2}, d_{xz}, and d_{yz}) having an orientation toward the *z* direction in the horizontal Ru_2 double atom played an important role in determining the NH_2 adsorption process, while for the inclined pentagon M double atom [RuFe, RuSc, and RuMn, where each Ru and M (Fe, Sc, and Mn) atom has a substantially different *z* position in the normal direction of the *x*–*y* plane], the d_{xz} and d_{xy} orbitals were found to be essential for the modification of NH_2 binding energy.

Our theoretical study provides the fundamental mechanism of NH_3 production catalysis on hetero-double atom catalysts and gives physical and chemical intuition (in particular, interplay of strain, dopant and configurational effects) for next generation multi-metallic atom catalysts for hydrogen storage applications.

Author contributions

The manuscript was written through contributions of all authors. All authors have given approval to the final version of the manuscript.

Conflicts of interest

There are no conflicts to declare.

Acknowledgements

This work was financially supported by the National Research Foundation of Korea (NRF) grant funded by the Korea government (MSIT) (No. NRF-2020R1A2C1099711 and NRF-2018M1A2A2061975). This work was also supported by the National Supercomputing Center with supercomputing resources including technical support (KSC-2021-CRE-0264).

Notes and references

1 H.-J. Neef, International overview of hydrogen and fuel cell research, *Energy*, 2009, **34**, 327–333.
2 L. van Biert, M. Godjevac, K. Visser and P. V. Aravid, A review of fuel cell systems for maritime applications, *J. Power Sources*, 2016, **327**, 345–364.
3 J. W. Pratt, L. E. Klebanoff, K. Munoz-Ramos, A. A. Akhil, D. B. Curgus and B. L. Schenkman, Proton exchange membrane fuel cells for electrical power generation on-board commercial airplanes, *Appl. Energy*, 2013, **101**, 776–796.
4 F. Ustolin and R. Taccani, Fuel cells for airborne usage: energy storage comparison, *Int. J. Hydrogen Energy*, 2018, **43**, 11853–11861.
5 S. S. Kumar and V. Himabindu, Hydrogen production by PEM water electrolysis – a review, *Mater. Sci. Energy Technol.*, 2019, **2**, 442–454.
6 F. Jiao and B. Xu, Electrochemical ammonia synthesis and ammonia fuel cells, *Adv. Mater.*, 2019, **31**, 1805173.
7 C. Zamfirescu and I. Dincer, Ammonia as a green fuel and hydrogen source for vehicular applications, *Fuel Process. Technol.*, 2009, **90**, 729–737.
8 R. Metkemeijer and P. Achard, Ammonia as a feedstock for a hydrogen fuel cell; reformer and fuel cell behaviour, *J. Power Sources*, 1994, **49**, 271–282.
9 W. Wang, J. M. Herreros, A. Tsolakis and A. P. E. York, Ammonia as hydrogen carrier for transportation; investigation of the ammonia exhaust gas fuel reforming, *Int. J. Hydrogen Energy*, 2013, **38**, 9907–9917.
10 C. H. Christensen, T. Johannessen, R. Z. Sørensen and J. K. Nørskov, Towards an ammonia-mediated hydrogen economy?, *Catal. Today*, 2006, **111**, 140–144.
11 V. Kyriakou, I. Garagounis, A. Vourros, E. Vasileiou and M. Stoukides, An electrochemical Haber-Bosch process, *Joule*, 2020, **4**, 142–158.
12 J. Hymphreys, R. Lan and S. Tao, Development and recent progress on ammonia synthesis catalysts for Habor-Bosch process, *Advanced Energy and Sustainability Research*, 2021, **2**, 2000043.
13 J. Kong, A. Lim, C. Yoon, J. H. Jang, H. C. Ham, J. Han, S. Nam, D. Kim, Y.-E. Sung, J. Choi and H. S. Park, Electrochemical synthesis of NH_3 at low temperature and atmospheric pressure using a γ-Fe2O3 catalyst, *ACS Sustainable Chem. Eng.*, 2017, **5**, 10986–10995.
14 N. Saadatjou, A. Jafari and S. Sahebdelfar, Ruthenium nanocatalysts for ammonia synthesis: a review, *Chem. Eng. Commun.*, 2018, **202**, 420–448.
15 N. Cao and G. Zheng, Aqueous electrocatalytic N_2 reduction under ambient conditions, *Nano Res.*, 2008, **11**, 2992–3008.
16 S. Giddey, S. P. S. Badwal and A. Kulkarni, Review of electrochemical ammonia production technologies and materials, *Int. J. Hydrogen Energy*, 2019, **38**, 14576–14594.
17 J. K. Nørskov, Electronic factors in catalysis, *Prog. Surf. Sci.*, 1991, **38**, 103–144.
18 H. Iriawan, S. Z. Andersen, X. Zhang, B. M. Comer, J. Barrio, P. Chen, A. J. Medford, I. E. L. Stephens, I. Chorkendorff and Y. Shao-Horn, Methods for nitrogen activation by reduction and oxidation, *Nature Reviews Methods Primers*, 2021, **1**, 56.
19 L. Forni, D. Molinari, I. Rossetti and N. Pernicone, Carbon-supported promoted Ru catalyst for ammonia synthesis, *Appl. Catal., A*, 1999, **185**, 269–275.
20 G. Ertl, Primary steps in catalytic synthesis of ammonia, *J. Vac. Sci. Technol., A*, 1983, **1**, 1247–1253.
21 V. Kordali, G. Kyriacou and C. Lambrou, Electrochemical synthesis of ammonia at atmospheric pressure and low temperature in a solid polymer electrolyte cell, *Chem. Commun.*, 2000, **17**, 1673–1674.
22 K. Imamura and J. Kubota, Electrochemical membrane cell for NH_3 synthesis from N_2 and H_2O by electrolysis at 200 to 250 °C using a Ru catalyst, hydrogen-permeable Pd membrane and phosphate-based electrolyte, *Sustainable Energy Fuels*, 2018, **2**, 1278–1286.
23 K. Kugler, M. Luhn, J. A. Schramm, K. Rahimi and M. Wessling, Galvanic deposition of Rh and Ru on randomly structured Ti felts for the electrochemical NH_3 synthesis, *Phys. Chem. Chem. Phys.*, 2015, **17**, 3768–3782.
24 G. Marnellos, S. Zisekas and M. Stoukides, Synthesis of ammonia at atmospheric pressure with the use of solid state proton conductors, *J. Catal.*, 2000, **193**, 80–87.
25 J. Wang, L. Yu, L. Hu, G. Chen, H. Xin and X. Feng, Ambient ammonia synthesis via palladium-catalyzed electrohydrogenation of dinitrogen at low over-potential, *Nat. Commun.*, 2018, **9**, 1795.
26 S. Li, D. Bao, M.-M. Shi, B.-R. Wulan, J.-M. Yan and Q. Jiang, Amorphizing of Au nanoparticles by CeOx–RGO hybrid support towards highly efficient electrocatalyst for N_2 reduction under ambient conditions, *Adv. Mater.*, 2017, **29**, 1700001.

27 R. Manjunatha and A. Schechter, Electrochemical synthesis of ammonia using ruthenium–platinum alloy at ambient pressure and low temperature, *Electrochem. Commun.*, 2018, **90**, 96–100.
28 Y. Abghoui and E. Skúlason, Computational predictions of catalytic activity of zincblende (110) surfaces of metal nitrides for electrochemical ammonia synthesis, *J. Phys. Chem. C*, 2017, **121**, 6141–6151.
29 M.-M. Shi, D. Bao, B.-R. Wulan, Y.-H. Le, Y.-F. Zhang, J.-M. Yan and Q. Jiang, Au Sub-nanoclusters on TiO2 toward highly efficient and selective electrocatalyst for N_2 conversion to NH_3 at ambient conditions, *Adv. Mater.*, 2017, **29**, 1606550.
30 S. Chen, S. Perathoner, C. Ampelli, C. Mebrahtu, D. Su and G. Centi, Electrocatalytic Synthesis of Ammonia at Room Temperature and Atmospheric Pressure from Water and Nitrogen on a Carbon-Nanotube-Based Electrocatalyst, *Angew. Chem., Int. Ed.*, 2017, **56**, 2699–2703.
31 X. Zhao, F. Yin, N. Liu, G. Li, T. Fan and B. Chen, Highly efficient metal–organic-framework catalysts for electrochemical synthesis of ammonia from N_2 (air) and water at low temperature and ambient pressure, *J. Mater. Sci.*, 2017, **52**, 10175–10185.
32 K. Kim, C.-Y. Yoo, J.-N. Kim, H. C. Yoon and J.-I. Han, Electrochemical synthesis of ammonia from water and nitrogen in ethylenediamine under ambient temperature and pressure, *J. Electrochem. Soc.*, 2016, **163**, F1523–F1526.
33 D. Yang, T. Chen and Z. Wang, Electrochemical reduction of aqueous nitrogen (N_2) at a low over-potential on (110)-oriented Mo nanofilm, *J. Mater. Chem. A*, 2017, **5**, 18967–18971.
34 L. Zhang, X. Ji, X. Ren, Y. Ma, X. Shi, Z. Tian, A. M. Asiri, L. Chen, B. Tang and X. Sun, Electrochemical ammonia synthesis via nitrogen reduction reaction on a MoS2 satalyst: theoretical and experimental studies, *Adv. Mater.*, 2018, **30**, 1800191.
35 X. Zhang, R.-M. Kong, H. Du, L. Xia and F. Qu, Highly efficient electrochemical ammonia synthesis via nitrogen reduction reactions on a VN nanowire array under ambient conditions, *Chem. Commun.*, 2018, **54**, 5323–5325.
36 X. Ma, J. Hu, M. Zheng, D. Li, H. Lv, H. He and C. Huang, N_2 reduction using single transition-metal atom supported on defective WS2 monolayer as promising catalysts: A DFT study, *Appl. Surf. Sci.*, 2019, **489**, 684–692.
37 Y. Liu, Y. Su, X. Quan, X. Fan, S. Chen, H. Yu, H. Zhao, Y. Zhang and J. Zhao, Facile ammonia synthesis from electrocatalytic N_2 reduction under ambient conditions on N-doped porous carbon, *ACS Catal.*, 2018, **8**, 1186–1191.
38 C. Lv, Y. Qian, C. Yan, Y. Ding, Y. Liu, G. Chen and G. Yu, Defect Engineering Metal-Free Polymeric Carbon Nitride Electrocatalyst for Effective Nitrogen Fixation under Ambient Conditions, *Angew. Chem., Int. Ed.*, 2018, **57**, 10246–10250.
39 S. Mukherjee, D. A. Cullen, S. Karakalos, K. Liu, H. Zhang, S. Zhao, H. Xu, K. L. More, G. Wang and G. Wu, Metal-organic framework-derived nitrogen-doped highly disordered carbon for electrochemical ammonia synthesis using N_2 and H_2O in alkaline electrolytes, *Nano Energy*, 2018, **48**, 217–226.
40 J. Zhao and Z. Chen, Single Mo atom supported on defective boron nitride monolayer as an efficient electrocatalyst for nitrogen fixation: a computational study, *J. Am. Chem. Soc.*, 2017, **139**, 12480–12487.
41 B. Huang, N. Li, W.-J. Ong and N. Zhou, Single atom-supported MXene: how single-atomic-site catalysts tune the high activity and selectivity of electrochemical nitrogen fixation, *J. Mater. Chem. A*, 2019, **7**, 27620–27631.
42 F. Lü, S. Zhao, R. Guo, J. He, X. Peng, H. Bao, J. Fu, L. Han, G. Qi, J. Luo, X. Tang and X. Liu, Nitrogen-coordinated single Fe sites for efficient electrocatalytic N_2 fixation in neutral media, *Nano Energy*, 2019, **61**, 420–427.
43 B. Qiao, A. Wang, X. Yang, L. F. Allard, Z. Jiang, Y. Cui, J. Liu, J. Li and T. Zhang, Single-atom catalysis of CO oxidation using Pt1/FeOx, *Nat. Chem.*, 2011, **3**, 634–641.
44 K. Liu, Y. Lei and G. Wang, Correlation between oxygen adsorption energy and electronic structure of transition metal macrocyclic complexes, *J. Chem. Phys.*, 2013, **139**, 204306.
45 C. Liu, Q. Li, J. Zhang, Y. Jin, D. R. MacFarlane and C. Sun, Conversion of dinitrogen to ammonia on Ru atoms supported on boron sheets: a DFT study, *J. Mater. Chem. A*, 2019, **7**, 4771–4776.
46 C. Choi, S. Back, N. Kim, J. Lim, Y. Kim and Y. Jung, Suppression of hydrogen evolution reaction in electrochemical N_2 reduction using single-atom catalysts: a computational guideline, *ACS Catal.*, 2018, **8**, 7517–7525.
47 Z. Geng, Y. Liu, X. Kong, P. Li, K. Li, Z. Liu, J. Du, M. Shu, R. Si and J. Zeng, Achieving a Record-High Yield Rate of 120.9 μgNH_3 mgcat.-1 h-1 for N_2 Electrochemical Reduction over Ru Single-Atom Catalysts, *Adv. Mater.*, 2018, **30**, 1803498.
48 R. Burch, Importance of ligand effects in metal alloy catalysts, *Acc. Chem. Res.*, 1982, **15**, 24–31.
49 B. Li, J. Wang, X. Gao, C. Qin, D. Yang, H. Lv, Q. Xiao and C. Zhang, High performance octahedral PtNi/C catalysts investigated from rotating disk electrode to membrane electrode assembly, *Nano Res.*, 2019, **12**, 281–287.
50 S. Kim, J. Jung, E. Yang, K.-Y. Lee and D. J. Moon, Hydrogen production by steam reforming of biomass-derived glycerol over Ni-based catalysts, *Catal. Today*, 2014, **228**, 145–151.
51 P. Hohenberg and W. Kohn, Inhomogeneous electron gas, *Phys. Rev.*, 1964, **136**, B864–B871.
52 W. Kohn and J. Sham, Self-consistent equations including exchange and correlation effects, *Phys. Rev.*, 1965, **140**, A1133–A1138.
53 G. Kresse and J. Furthmüller, Efficient iterative schemes for ab initio total-energy calculations using a plane-wave basis set, *Phys. Rev. B: Condens. Matter Mater. Phys.*, 1996, **124**, 11169–11186.
54 P. E. Blöchl, Projector augmented-wave method, *Phys. Rev. B: Condens. Matter Mater. Phys.*, 1994, **50**, 17953–17979.
55 J. P. Perdew, K. Burke and M. Ernzerhof, Generalized gradient approximation made simple, *Phys. Rev. Lett.*, 1996, **77**, 3865–3868.

56 F. P. Bundy and J. S. Kasper, Hexagonal diamond—a new form of carbon, *J. Chem. Phys.*, 1967, **46**, 3437–3446.

57 H. Sevinçli, M. Topsakal, E. Durgun and S. Ciraci, Electronic and Magnetic Properties of 3d Transition-Metal Atom Adsorbed Graphene and Graphene Nanoribbons, *Phys. Rev. B: Condens. Matter Mater. Phys.*, 2008, **77**, 195434.

58 Z. He, K. He, A. W. Robertson, A. I. Kirkland, D. Kim, J. Ihm, E. Yoon, G.-D. Lee and J. H. Warner, Atomic Structure and Dynamics of Metal Dopant Pairs in Graphene, *Nano Lett.*, 2014, **14**, 3766–3772.

59 Y. Li, H. Su, S. H. Chan and Q. Sun, CO2 Electroreduction Performance of Transition Metal Dimers supported on Graphene: A Theoretical Study, *ACS Catal.*, 2015, **5**, 6658–6664.

60 A. W. Robertson, C. S. Allen, Y. A. Wu, K. He, J. Olivier, J. Neethling, A. I. Kirkland and J. H. Warner, Spatial Control of Defect Creation in Graphene at the Nanoscale, *Nat. Commun.*, 2012, **3**, 1144.

61 H. Yan, Y. Lin, H. Wu, W. Zhang, Z. Sun, H. Cheng, W. Liu, C. Wang, J. Li, X. Huang, T. Yao, J. Yang, S. Wei and J. Lu, Bottom-up precise synthesis of stable platinum dimers on graphene, *Nat. Commun.*, 2017, **8**, 1070.

62 H. Jiang and W. Yang, Conjugate-gradient optimization method for orbital-free density functional calculations, *J. Chem. Phys.*, 2004, **121**, 2030–2036.

63 P. E. Blöchl, O. Jepsen and O. K. Anderson, Improved tetrahedron method for Brillouin-zone integrations, *Phys. Rev. B: Condens. Matter Mater. Phys.*, 1994, **49**, 16223–16233.

64 J. K. Nørskov, J. Rossmeisl, A. Logadottir, L. Lindqvist, J. R. Kitchin, T. Bligaard and H. Jónsson, Origin of the over-potential for oxygen reduction at a fuel-cell cathode, *J. Phys. Chem. B*, 2004, **108**, 17886–17892.

65 E. Skúlason, V. Tripkovic, M. E. Björketun, S. Gudmundsdóttir, G. Karlberg, J. Rossmeisl, T. Bligaard, H. Jónsson and J. K. Nørskov, Modeling the electrochemical hydrogen oxidation and evolution reactions on the basis of density functional theory calculations, *J. Phys. Chem. C*, 2010, **114**, 18182.

66 *NIST Standard Reference Database Number 69*, https://webbook.nist.gov/chemistry/.

67 Y. Abghoui, A. L. Garden, J. G. Howalt, T. Vegge and E. Skúlason, Electroreduction of N_2 to ammonia at ambient conditions on mononitrides of Zr, Nb, Cr, and V: a DFT guide for experiments, *ACS Catal.*, 2016, **6**, 635–646.

68 X. Li, Q. Li, J. Cheng, L. Liu, Q. Yan, Y. Wu, X. Zhang, Z. Wang, Q. Qiu and Y. Luo, Conversion of dinitrogen to ammonia by FeN3-embedded graphene, *J. Am. Chem. Soc.*, 2016, **138**, 8706–8709.

69 H. Niu, X. Wang, C. Shao, Z. Zhang and Y. Guo, Computational Screening Single-Atom Catalysts Supported on g-CN for N2 Reduction: High Activity and Selectivity, *ACS Sustainable Chem. Eng.*, 2020, **8**, 13749–13758.

70 X. Zhai, L. Li, X. Liu, Y. Li, J. Yang, D. Yang, J. Zhang, H. Yan and G. Ge, A DFT screening of single transition atoms supported on MoS2 as highly efficient electrocatalysts for the nitrogen reduction reaction, *Nanoscale*, 2020, **12**, 10035–10043.

71 Z. Xu, R. Song, M. Wang, X. Zhang, G. Liu and G. Qiao, Single atom-doped arsenene as electrocatalyst for reducing nitrogen to ammonia: a DFT study, *Phys. Chem. Chem. Phys.*, 2020, **22**, 26223–26230.

72 M. Mavrikakis, B. Hammer and J. K. Nørskov, Effect of Strain on the Reactivity of Metal Surfaces, *Phys. Rev. Lett.*, 1998, **81**, 2819–2822.

73 P. Strasser, S. Koh, T. Anniyev, J. Greeley, K. More, C. Yu, Z. Liu, S. Kaya, D. Nordlund, H. Ogasawara, M. F. Toney and A. Nilsson, Lattice-strain control of the activity in dealloyed core–shell fuel cell catalysts, *Nat. Chem.*, 2010, **2**, 454–460.

74 A. Khorshidi, J. Violet, J. Hashemi and A. A. Peterson, How strain can break the scaling relations of catalysis, *Nat. Catal.*, 2018, **1**, 263–268.

75 T. Bligaard and J. K. Nørskov, Ligand effects in heterogeneous catalysis and electrochemistry, *Electrochim. Acta*, 2007, **52**, 5512–5516.

76 A. A. Jeffery, S.-Y. Lee, J. Min, Y. Kim, S. Lee, J. H. Lee, N. Jung and S. J. Yoo, Surface engineering of Pd-based nanoparticles by gas treatment for oxygen reduction reaction, *Korean Journal of Chemical Engineering*, 2020, **37**(8), 1360–1364.

